

# MAELi - Masked Autoencoder for Large-Scale LiDAR Point Clouds

Georg Krispel<sup>1</sup> David Schinagl<sup>1,2</sup> Christian Fruhwirth-Reisinger<sup>1,2</sup> Horst Possegger<sup>1</sup> Horst Bischof<sup>1,2</sup>

{georg.krispel,david.schinagl,christian.reisinger,possegger,bischof}@icg.tugraz.at

<sup>1</sup> Graz University of Technology <sup>2</sup> Christian Doppler Laboratory for Embedded Machine Learning

## Abstract

We demonstrate how the often overlooked inherent properties of large-scale LiDAR point clouds can be effectively utilized for self-supervised representation learning. In pursuit of this goal, we design a highly data-efficient feature pre-training backbone that considerably reduces the need for tedious 3D annotations to train state-of-the-art object detectors. We propose Masked AutoEncoder for LiDAR point clouds (MAELi) that intuitively leverages the sparsity of LiDAR point clouds in both the encoder and decoder during reconstruction. Our approach results in more expressive and useful features, which can be directly applied to downstream perception tasks, such as 3D object detection for autonomous driving. In a novel reconstruction schema, MAELi distinguishes between free and occluded space and employs a new masking strategy that targets the LiDAR's inherent spherical projection. To demonstrate the potential of MAELi, we pre-train one of the most widely-used 3D backbones in an end-to-end manner and show the effectiveness of our unsupervised pre-trained features on various 3D object detection architectures. Our method achieves significant performance improvements when only a small fraction of labeled frames is available for fine-tuning object detectors. For instance, with  $\sim 800$  labeled frames, MAELi features enhance a SECOND model by +10.79APH/LEVEL 2 on Waymo Vehicles.

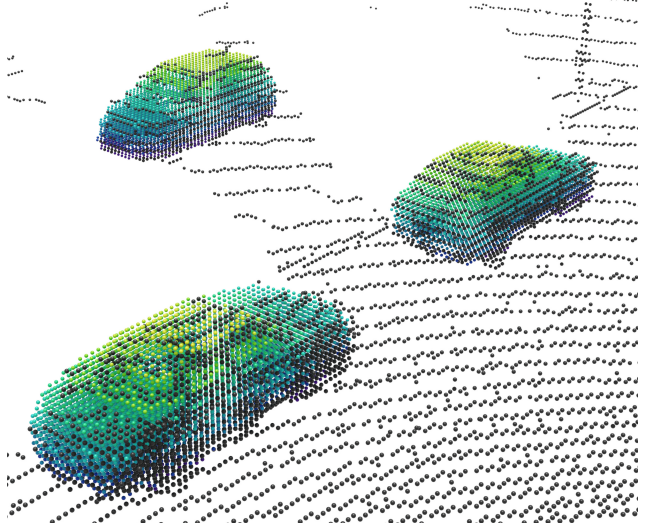


Figure 1: Reconstructed point cloud. In contrast to existing self-supervised representation learning (SSRL) approaches which simply reconstruct the initial point cloud (black), MAELi learns an expressive feature representation which captures the full geometric object structure of objects, without any ground truth labels. For visualization purposes, we color-coded the points by their  $z$ -coordinate and removed the reconstructed ground plane.

## 1. Introduction

Thanks to recent large-scale and elaborately curated datasets, like the Waymo Open Dataset [47], we have seen tremendous progress in a variety of 3D perception tasks for autonomous driving. However, even with such cost-intensive datasets, models are only transferable to other domains with significant performance drops [54].

Self-supervised representation learning (SSRL) provides a technique to reduce the costly labeling effort. The overall idea is to learn a universal feature representation in an unsupervised way, that is later utilized for a specific downstream task, such as object detection. One of the most common

approaches in 3D is to learn representations via *point cloud reconstruction* [1, 30, 37, 52, 56, 73]. There, the task is to restore removed parts of a point cloud and thereby learning an implicit understanding of the scene and the object's inner geometric structure. This is especially useful for full 3D point clouds generated from CAD models, such as ModelNet [57] or ShapeNet [7]. Recently, these methods were adapted for large-scale point clouds within the automotive domain [19, 36], already showing promising results.

Existing SSRL approaches, however, neglect several inherent, but fundamental properties of LiDAR point clouds. Contrary to previous methods, we leverage these properties and propose *MAELi*, a transformer-less masked autoencoder (MAE). For this, we do not follow the straightforward

approach of reconstructing the occupied space. Instead, we present a novel reconstruction schema that allows us to go beyond the (visible) LiDAR points. As a result, MAELi learns how objects look like from any viewing direction, implicitly and in a genuinely unsupervised way, as illustrated in Figure 1.

Intuitively, we explicitly distinguish *occupied*, *free* and *unknown* space. While free space must be traversable and occupied space must reflect the respective LiDAR beams, we cannot make any assumptions about unknown space. Therefore, we do not induce any self-supervision in these regions during reconstruction. In other words, our SSRL schema does not penalize the completion of structures in unknown regions which are either occluded or insufficiently sampled due to the limited LiDAR resolution.

During training, the model sees a large amount of objects, both in various poses and differently sampled. Despite the missing labels, our unique objective allows the model to reconstruct whole objects, *i.e.* implicitly capturing the entire geometric structure. In the process, MAELi learns features which better coincide with the underlying geometric structure instead of simply learning how to precisely reconstruct a masked point cloud surface (and thus, not learning the geometric contextual information).

For evaluation, we select the most critical automotive perception task, *i.e.* object detection. Our memory-efficient, sparse decoder structure enables efficient pre-training of state-of-the-art object detectors in an end-to-end fashion on a single GPU. In extensive experiments on the Waymo Open Dataset [47], KITTI 3D [12] and ONCE [32] we demonstrate that MAELi features are well suited to effectively pre-train several state-of-the-art 3D detectors while requiring only a tiny fraction of labeled data.

In summary, our contributions are threefold:

- We propose a LiDAR-aware SSRL schema to pre-train an encoder applicable to a variety of state-of-the-art 3D object detectors.
- We introduce a novel masking strategy and reconstruction loss for unsupervised representation learning, especially designed for LiDAR properties.
- We show the effectivity of our pre-trained features improving several baselines, significantly when labeled data is scarce.

## 2. Related Work

**LiDAR-based 3D Object Detection:** Due to the rise of autonomous driving, formidable effort has been made researching and improving 3D object detection based on LiDAR point clouds. These methods can be divided on how the irregular structure of a point cloud is handled. *Point-based methods* [43, 45, 67, 74], initially inspired by the pio-

neering work of Qi *et al.* [38, 39], directly process points by means of their coordinates and input features, *e.g.* LiDAR reflectivity. Based on this, Shi *et al.* [43] introduce a two-stage detector including proposal generation and box refinement. Point-GNN [45] defines a graph, thereby grouping neighboring points within a fixed radius, before feeding it to a dedicated graph neural network.

*Grid-based methods* [25, 55, 63, 64, 72, 77] define a regular grid, which enables common operations, *e.g.* convolutions, already successfully applied to 2D imagery. Several approaches, *e.g.* [55, 64], project the data onto a birds-eye-view, whereas VoxelNet [77] employs 3D convolutions. However, the computational effort grows cubically in 3D, but LiDAR point clouds only cover a small fraction of the relevant space. Thus, SECOND [63] utilizes sparse operations to significantly speed up inference time and memory consumption. Reusing the encoder from SECOND, Centerpoint [72] adapts the idea from [76] and reformulates the problem of 3D detection as the extraction of keypoints, *i.e.* the bounding box centers.

By contrast, [2, 11, 26, 34] solely utilize a point cloud’s *range view*, as it is a compact and lossless representation enabling an efficient feature extraction akin to the one in 2D imagery. However, depending on its distance, a single object varies in scale within the range view, but a model should always produce the same-sized 3D bounding box. This discrepancy requires several adjustments [11].

*Hybrid methods* [16, 21, 27, 35, 41, 42, 44, 68, 69] combine aspects of both, point- and grid-based approaches. For example, PV-RCNN [41, 42] incorporates features, which are derived from the respective layers of the voxel encoder and directly from the point cloud itself. Part-A<sup>2</sup> [44] classifies each point’s relative position within a bounding box as an auxiliary task. Hu *et al.* [21] utilize the estimated point-density in order to redefine their voxel’s centroid position and improve the subsequent RoI Grid Pooling [41] as well as the confidence prediction of the bounding boxes. Despite these differences, all these methods share the same encoder initially introduced with SECOND [63].

More recently, *Transformers* [51] were adapted to LiDAR-based 3D object detection [15, 31, 33, 40, 48, 65]. Whilst achieving great results, vanilla Transformers usually have a large memory footprint and require a lot of processing power. In order to process large LiDAR point clouds, various tweaks mitigate the quadratically growing complexity depending on the number of input points. Sun *et al.* [48] even achieve real-time performance during inference with a highly optimized version of their SWFormer. Nevertheless, either a dataset of substantial size or a proper pre-training strategy is still needed.

**SSRL for 2D Imagery and Points Clouds:** Self-supervised representation learning strives to learn useful features before introducing any supervision in the form of

manually labeled ground truth data. These features are utilized to improve the results on respective downstream tasks or reduce the amount of required training data.

*Contrastive learning* approaches task a model to maintain similar embeddings for the same data instance when transformed with different augmentations. Consequently, different data instances should lead to diverging embeddings. Initially applied to 2D imagery [8, 18, 20, 53], these methods were also adapted for point clouds [23, 28, 59, 71, 75]. Naturally, the granularity of the induced consistency loss defines the *semantic level* on which the model agrees upon. In other words, contrastive learning on a global embedding describing an entire image or point cloud is more suitable for downstream tasks like classification. Tasks like object detection or semantic segmentation, however, necessitate a more fine-grained treatment. The causality dilemma is to sample semantically coherent regions with a proper level of detail without knowing what is semantically coherent. For example, Yin *et al.* [71] generate proposals via farthest point sampling and ball queries after removing the ground plane.

**SSRL via Reconstruction:** Recently, generative self-supervised representation learning approaches are on the rise, outperforming their contrastive counterparts. One of the most successful concepts is the one of *denoising autoencoders*. Based on the encoder’s output embedding, the decoder is tasked to reconstruct the denoised input and if successful, the encoder is forced to learn a useful representation resilient to noise. Especially the reconstruction of a masked input gained huge traction across various domains of application, among others like natural language processing (NLP) [10] and 2D imagery [17] also on point clouds. The major research focus, however, is to learn representations on synthetic datasets [13, 30, 37, 52, 62, 66, 73], *e.g.* ShapeNet [7] or ModelNet [57]. Just very recently a few works consider LiDAR point clouds [19, 36, 58].

Xie *et al.* [58] require full supervision, whereas we do not need any labels for pre-training. In [36], the authors pre-train the sparse 3D voxel backbone ignoring the dense birds-eye view (BEV) part of a common 3D encoder. They instead apply a computationally demanding dense decoder. In contrast, we propose a memory efficient sparse decoder, which enables us to pre-train the entire encoder.

Only very few works consider a LiDAR point cloud’s inherent properties, *i.e.* its sampling resolution and 2.5D perception (due to occlusion). Wang *et al.* [52] synthesized occlusion on small-scale full 3D point scans and learn to complete them, thereby pre-training useful features for several downstream tasks. Hu *et al.* [22] compute visibility maps via raycasting in order to avoid inconsistent object augmentation [63] and to be added as additional input to a detection network. Xu *et al.* [60] complete points of ground truth objects by grouping similar ones and use them to learn an aux-

iliary task, which estimates the probability of an occluded area to be occupied by an object.

Concurrent to our work, ALSO [3] proposes SSRL via surface interpolation. It generates query points along LiDAR rays that are situated in front and slightly behind the detected hits and instruct the network to predict the occupancy of these selected points while treating occluded areas as occupied. The objective of this self-supervised task is deemed achieved once the network is able to interpolate the underlying surface. While the resulting feature representation already shows promising results, our LiDAR-aware reconstruction demonstrates further improvements as our model inherently captures the whole object geometry.

Several approaches use point cloud completion as a pre-processing step rather than learning a representation, *e.g.* [50, 61]. In [50], the authors complete a LiDAR point cloud to transform it into a canonical form for a 3D object detector. However, this requires either synthetic or ground truth labels for training and, during inference, an elaborate network on top of the detector.

### 3. MAE for Large-scale LiDAR Point Clouds

We aim to significantly reduce the expensive labeling effort for large-scale LiDAR point clouds via self-supervised representation learning (SSRL). We build upon the successful masking and reconstruction paradigm, but observed that existing approaches only learn to reconstruct the original input point cloud, nothing more. While this is well suited for full 3D models, such as those generated by CAD renderings [7, 57], this approach limits the usefulness of the learned features for LiDAR point clouds in two key aspects. First, the limited angular resolution of a LiDAR sensor induces gaps between the LiDAR beams. Simply reconstructing the original point cloud would mean to penalize the model for (correctly) reconstructed points in these gaps. Second, a LiDAR sensor can not capture objects fully. Once a surface reflects a beam, there is no spatial information from behind the surface. Thus, models based on standard reconstruction are hindered from learning implicit contextual information. With MAELi, we observed that this implicit information results in more expressive features.

To allow simple integration into a wide variety of state-of-the-art models, we demonstrate MAELi to pre-train one of the most widely used point cloud encoders today, initially introduced by SECOND [63]. In the following, we briefly summarize the overall encoder structure (Sec. 3.1) before we explain our sparse decoder (Sec. 3.2), the reconstruction objective (Sec. 3.3) and our masking strategy (Sec. 3.4).

**Definitions & Notations:** Let  $\mathcal{V}^{E,s} = \{\mathbf{v}_j^{E,s}\}_{j=1\dots M^{E,s}}$  be the  $M^{E,s}$  active voxel positions of a certain tensor stride  $s$  in the sparse encoder and  $\mathcal{V}^{D,s} = \{\mathbf{v}_j^{D,s}\}_{j=1\dots M^{D,s}}$  the  $M^{D,s}$  active voxel positions in the sparse decoder,

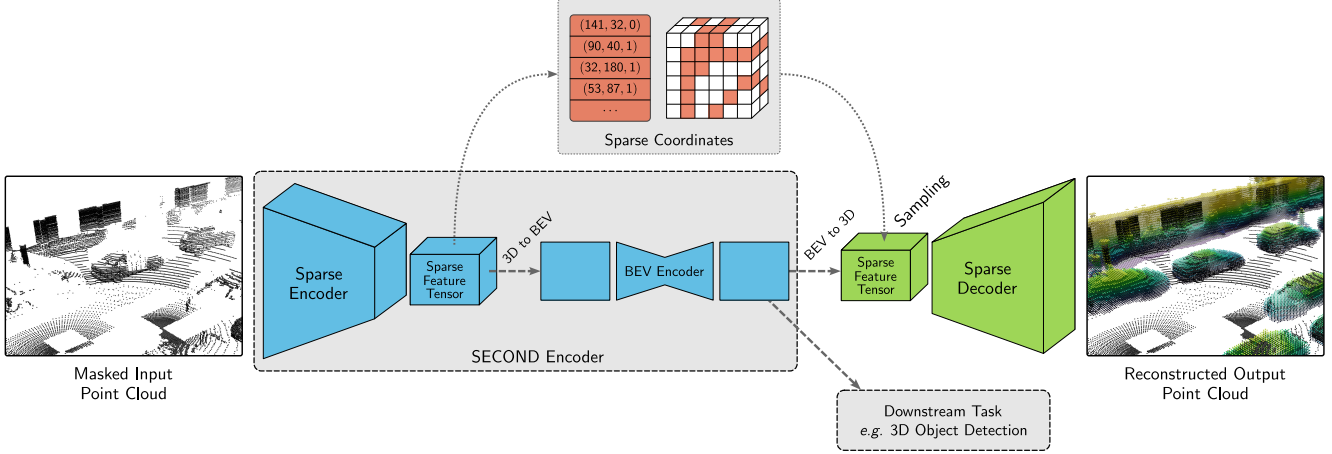


Figure 2: Overview of our MAELi pre-training. The task of our sparse decoder (green) is to reconstruct the missing parts of the masked input point cloud. Thereby, the encoder (blue) is forced to learn a reasonable representation usable for a downstream task, *e.g.* 3D object detection. Since we do not penalize our network for reconstructing voxels at areas not visible to the LiDAR, it learns to reconstruct occluded parts without any ground truth labels, leading to more expressive features. We color coded the  $z$ -coordinate and removed the ground plane in the output for visualization purposes.

where  $\mathbf{v}_j \in \mathbb{R}^3$ . A voxel position is considered *active* if any of its related features deviates from zero and is thus taken into account by the sparse operations. Only the active sites are actually stored in memory.

We follow the notation of [9] for sparse convolutions, where the *voxel/tensor stride*  $s$  refers to the distance between two voxels w.r.t. the highest voxel resolution along each axis. For example, applying two (or three) 3D convolutions with a stride of 2 leads to a feature map with a tensor stride of 4 (or 8). Consequently,  $\mathcal{V}^{E,1}$  and  $\mathcal{V}^{D,1}$  denote the voxels in the encoder’s input layer and the final output layer of the decoder, respectively. A downsampling step increases the stride, while an upsampling step decreases it.

### 3.1. Sparse 3D and BEV Encoder

We use MAELi to pre-train the features of the widely used SECOND [63] encoder, as illustrated in Figure 2. This encoder first voxelizes the point cloud and processes the sparse data via dedicated sparse convolutions (SC). Contrary to its dense pendant, a SC is only applied if the kernel covers any active site. Nevertheless, even with small  $3 \times 3$  kernels, these active sites dilute rapidly, increasing computational effort on the way. Thus, SECOND additionally includes submanifold sparse convolutions (SSC) [14], where the kernel center is only placed on the active sites. It only considers active sites covered by the kernel and maintains their amount and a favorable memory consumption.

After multiple downsampling steps, the spatially reduced voxel space and its features are transformed to a dense tensor, projected to a BEV representation and processed by a common small 2D encoder/decoder structure to increase the receptive field. The resulting features then act as inputs to

the detection heads of various state-of-the-art models.

### 3.2. Sparse Reconstruction Decoder

Our goal is to obtain more expressive features via pre-training the *entire* SECOND encoder, *i.e.* both the sparse 3D voxel backbone and the 2D BEV backbone, in an end-to-end fashion. Thus, we attach a reconstruction decoder as illustrated in Figure 2. The detailed architecture is given in the supplementary material. Contrary to existing sparse encoder/decoder structures for LiDAR point clouds, *e.g.* Part-A<sup>2</sup> [44], we have to address two key differences:

First, we want to pre-train the entire encoder such that it utilizes as much representation capabilities as possible. Therefore, we need to adapt to the dense feature map provided by the BEV backbone. However, dense upsampling to the original spatial resolution is not feasible, as it would be too demanding in terms of both memory and computational effort. Instead, we transform the dense feature map into a sparse tensor, guided by the active sites of the sparse encoder: we reshape the dense tensor such that its dimension coincide with the 3D output volume of the sparse encoder and sample certain coordinates, *i.e.* we subsequently set them active. In particular, we use the same coordinates which were active at the output of the sparse encoder and extract the respective features from the dense BEV output.

Second, to perform reconstruction on a point cloud, we require a decoder which is able to also restore the removed voxels. However, a common upsampling step by a factor of 2 applied to an active voxel would already generate 8 more fine-grained voxels with half size. To avoid memory issues due to the cubically increasing number of active voxels, existing approaches, such as [44], limit the upsampling



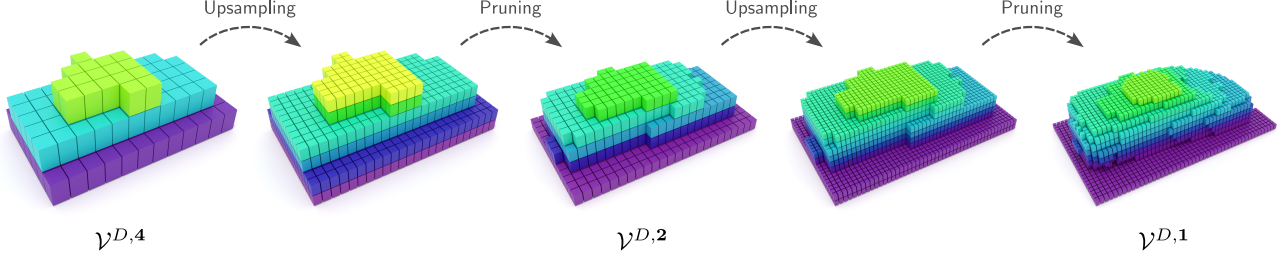


Figure 3: Reconstruction of a car within our decoder. An upsampling step halves the *voxel stride* and voxel size and increases the number of voxels. Subsequently, superfluous voxels are removed during the pruning step. We cropped the car and color coded the  $z$ -coordinate for visualization purposes.

layer such that only voxels are generated which were already active in the corresponding layer of the encoder. Consequently,  $\mathcal{V}^{E,s}$  would be equal to  $\mathcal{V}^{D,s}$  for all strides  $s$ . However, this strategy does not allow the decoder to recover voxels which were not present in the encoder, rendering it unusable for a reconstruction task.

We aim for a decoder that is able to reconstruct *and complete*, in order to capture the underlying geometry of the scene. Thus, we allow each upsampling layer to grow (cubically), but add a subsequent pruning layer that learns to remove redundant voxels, as illustrated in Figure 3. For this, we leverage the idea of small-scale point cloud reconstruction [9] and apply a  $1 \times 1$  convolution to the sparse feature map that learns the pruning. To obtain stronger feature representations, we propose an extended reconstruction objective in the following.

### 3.3. Reconstruction Objective

We design our reconstruction objective to induce more knowledge about the underlying structure of the perceived environment. Intuitively, it should be easier for a model to learn what an entire car looks like instead of simply reconstructing the specific points sensed by the LiDAR beams. Therefore, we distinguish three categories of voxels: *occupied*, *free* and *unknown*. They are illustrated in Figure 4.

Occupied voxels contain surface points from the original point cloud (before masking) and should thus be part of the reconstruction. Free voxels are the ones traversed by the LiDAR beam without hitting any surface and thus, should remain empty. Finally, we categorize a voxel as *unknown* if neither of the first two cases applies, *i.e.* these are either occluded or were not sensed by the beam due to the limited angular resolution. This categorization enables the reconstruction to grow beyond the initially sensed point cloud.

We observe that the discrete voxelization can cause inaccuracies, especially at low resolution voxel grids. We mitigate this by decreasing the loss of a free voxel via the normal distance  $d_j^{D,s}$  between its voxel center  $\mathbf{v}_j^{D,s}$  and the nearest LiDAR beam. More formally, we define the weight

$w_j^{D,s}$  for a voxel as

$$w_j^{D,s} = \begin{cases} 0 & \text{if } \mathbf{v}_j^{D,s} \text{ is } \textit{unknown}, \\ 1 & \text{if } \mathbf{v}_j^{D,s} \text{ is } \textit{occupied}, \\ 1 - \frac{2 d_j^{D,s}}{d_v^s} & \text{if } \mathbf{v}_j^{D,s} \text{ is } \textit{free}, \end{cases} \quad (1)$$

where  $d_v^s$  denotes the length of a voxel diagonal at stride  $s$ .

We require the same categorization for voxels of lower resolution and larger strides, respectively. For example, a voxel of stride  $s$  spatially covers eight voxels of stride  $s/2$  after upsampling (see Figure 3). Here, however, we

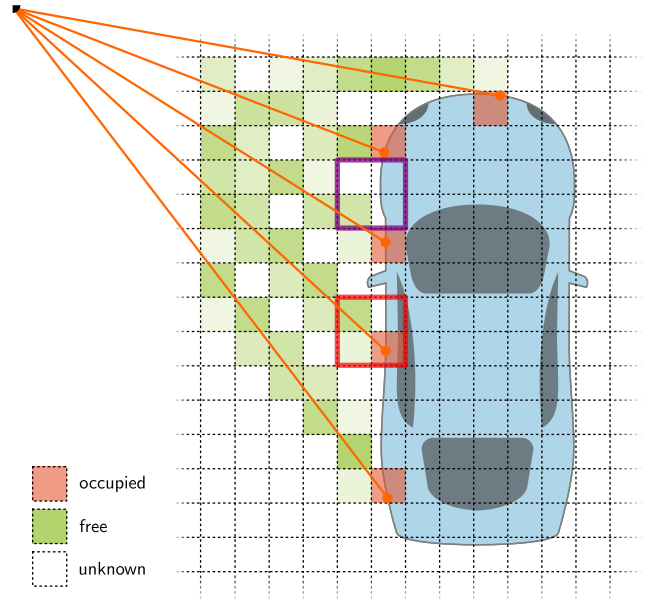


Figure 4: A loss should only be induced for voxels, where we *actually know* whether the space is free or not. LiDAR beams traverse *free* voxels (green) until they hit a surface, *i.e.* an *occupied* voxel (red). All other voxels are considered *unknown*. The loss for a *free* voxel is weighted by the proximity of its center to the nearest beam (different shades of green) to counter inaccuracies due to discrete voxelization.

need to consider that if a low-resolution voxel is pruned, it can no longer generate a self-supervision signal for its higher-resolution voxels during upsampling. Thus, a low-resolution voxel is considered *occupied* if it incorporates any high-resolution *occupied* voxel (red rectangle in Figure 4). Similarly, it is *unknown* (violet rectangle) if it incorporates any *unknown* voxel but no *occupied* ones. Otherwise, the low-resolution voxel is categorized as *free*.

In summary, the objective during self-supervised pre-training is to correctly classify whether a voxel is *occupied* or *free*, while not penalizing *unknown* ones. For this, we use a weighted binary cross-entropy loss

$$\mathcal{L} = -\frac{1}{\widetilde{M}^D} \sum_{\mathbf{s} \in \mathcal{S}^D} \sum_{j=1}^{M^{D,\mathbf{s}}} w_j^{D,\mathbf{s}} l_j^{D,\mathbf{s}}, \text{ with} \quad (2)$$

$$l_j^{D,\mathbf{s}} = \left[ y_j^{D,\mathbf{s}} \log x_j^{D,\mathbf{s}} + (1 - y_j^{D,\mathbf{s}}) \log(1 - x_j^{D,\mathbf{s}}) \right], \quad (3)$$

where  $\mathcal{S}^D$  denotes the set of all strides;  $\widetilde{M}^D$  is the amount of all *occupied* and *free* voxel in the decoder;  $y_j^{D,\mathbf{s}}$  is the actual occupancy of the voxelized input point cloud, *i.e.* 1 if  $\mathbf{v}_j^{d,\mathbf{s}}$  is *occupied* and 0 otherwise; and  $x_j^{D,\mathbf{s}}$  is our model’s predicted occupancy probability. In other words, we penalize each pruning step for removing *occupied* and maintaining *free* voxels, but we do not induce any loss for *unknown* voxels.

### 3.4. Masking Strategy

In methods applied to small-scale full 3D point clouds, a common masking strategy is to apply Farthest Point Sampling (FPS) and the K-Nearest Neighbor (KNN) algorithm to create overlapping patches [37, 73], which are then randomly removed. Applying FPS to LiDAR point clouds would, however, predominantly pick isolated points, which are usually single outliers far off. Masking these would not be beneficial to learn a strong feature representation, as such outliers usually do not correspond to real scene structures and have only few neighboring points. Instead, we exploit the voxelization step already in place and mask the voxels randomly.

Furthermore, consider the sampling resolution of a standard spinning LiDAR sensor: It sends out multiple beams, waits for their return and then derives the distance to a hit obstacle, *i.e.* the *range*, from the elapsed time. Every beam has an inclination and rotates around a common vertical axis, defining an azimuth. Since two specific beams enclose a constant angle, the spatial resolution and thus, the number of points decreases with the distance to the hit object. Considering SSRL via point cloud reconstruction, there is less self-supervision with increasing distance to the sensor.

Intuitively, if we remove points from nearby regions, such that they look similar to sparser regions further away, the model should be able to better generalize to these. We

incorporate this *spherical masking* idea by reducing the angular resolution in both, azimuth and inclination. To do this efficiently, we subsample the LiDAR’s range image. In particular, we randomly sample two integers  $1 \leq m_r, m_c \leq 4$  and filter all rows  $r$  and columns  $c$  of the range image for which  $r \bmod m_r \neq 0$  or  $c \bmod m_c \neq 0$ , respectively. For example, using only every second row and column halves the angular resolution. This way, an object is sampled as if it would have been further away, but we are able to induce stronger self-supervision during our reconstruction task.

## 4. Experiments

Our pre-training approach is evaluated on the challenging Waymo Open Dataset (WOD) [47], comprising 798 training sequences and 202 validation sequences. Labels are provided for Vehicles, Pedestrians, and Cyclists. We report our results using the official Waymo evaluation protocol, including AP and APH for the LEVEL 2 difficulty. Additionally, we showcase the transferability of our features to the KITTI 3D [12] and ONCE [32] datasets, with 3D object detection evaluation scores reported using 40 recall points ( $R_{40}$ ) for KITTI 3D and orientation-aware AP for ONCE.

**Implementation Details:** We integrate MAELi into the OpenPCDet [49] framework (v0.5.2) and employ the Minkowski Engine [9] to design our sparse decoder. We pre-train the encoder for 30 epochs without any labeled ground truth. We utilize the Adam optimizer [24] and a one-cycle policy [46] with a maximum learning rate of 0.003. To fine-tune the different detectors with our pre-trained features, we warmup the detection head by freezing the encoder for 5 epochs and train end-to-end according to the default OpenPCDet configuration. We ran our pre-training and subsequent experiments on an NVIDIA® GeForce® RTX 3090 GPU.

OpenPCDet provides several augmentation techniques for Waymo, *i.e.* random flip/rotation/scaling and *ground truth sampling* [63]. During pre-training, we utilize random flip/rotation/scaling in addition to our masking strategy (see Section 3.4). For fine-tuning, we adopt all of them, but we adjust *ground truth sampling* for a fair data efficiency evaluation as follows.

### 4.1. Data Efficiency & Transferability

Our ultimate goal is to significantly reduce the amount of labeled data needed to train state-of-the-art detectors. To this end, we demonstrate the benefits of using MAELi-pre-trained features for detectors in a low data regime as well as their transferability to other datasets.

**Pre-training Setting:** We split the Waymo training set into two groups. The first 399 sequences are used without any ground truth labels to pre-train our features. We then uniformly sample varying fractions of all remaining frames

Fraction	Method	3D AP/APH (LEVEL 2)									
		Gain		Overall		Vehicle		Pedestrian		Cyclist	
		AP	APH	AP	APH	AP	APH	AP	APH	AP	APH
1% (791 frames)	SECOND [63]	-	-	31.09	22.25	41.64	40.02	33.39	17.45	18.24	9.29
	+ MAELi	+14.92	+10.79	46.01	33.05	51.05	50.11	48.13	24.65	38.86	24.38
5% (3952 frames)	SECOND [63]	-	-	46.67	34.05	53.19	52.37	44.77	22.80	42.04	26.97
	+ ProfTeach [70]	+4.43	+11.70	51.10	45.75	53.04	52.54	50.33	38.67	49.92	46.03
	+ MAELi	+6.29	+13.94	52.96	47.99	57.50	56.75	53.45	41.27	47.93	45.94
10% (7904 frames)	SECOND [63]	-	-	52.74	38.23	58.11	57.46	52.26	28.15	47.85	29.07
	+ ProfTeach [70]	+2.27	+12.20	55.01	50.43	57.59	56.92	54.28	43.19	53.15	51.18
	+ MAELi	+3.23	+13.61	55.97	51.84	60.13	59.47	55.89	45.52	51.90	50.52
20% (15808 frames)	SECOND [63]	-	-	55.82	51.26	60.16	59.54	54.28	43.30	53.03	50.93
	+ ProfTeach [70]	+2.77	+2.90	58.59	54.16	59.97	59.36	57.88	46.97	57.93	56.15
	+ MAELi	+2.27	+2.75	58.09	54.01	61.80	61.21	57.91	47.63	54.57	53.18

Table 1: Quantitative results of our features on SECOND on the Waymo *val* set. We use the first 399 sequences of the Waymo *train* set for pre-training and different fractions of the latter 399 sequences for fine-tuning. ProficientTeachers, a semi-supervised method, employs random sampling on the data.

for fine-tuning. For a fair evaluation, we cannot apply the vanilla form of ground truth sampling from OpenPCDet, as it samples ground truth objects across the entire dataset and copy-pastes these randomly into frames which contain only few objects. Without change, this would add ground truth objects from other than our subsampled frames and thus, invalidate the data efficiency study. Thus, we filter the original ground truth database and ensure that it only contains objects from the actually used frames.

**Waymo Open Dataset:** We show the benefits of MAELi-pre-trained features in a low-data regime for SECOND [63] in Table 1, by using different fractions of labeled data from the latter 399 sequences to fine-tune the detection heads. We compare with ProficientTeachers [70], a state-of-the-art but semi-supervised approach for data-efficient 3D object detection (results for Centerpoint [72] and PV-RCNN [63] are provided in the supplementary material).

**KITTI 3D:** We maintain our pre-training scheme and apply our features to the KITTI 3D benchmark to demonstrate their transferability. Our results on a low-data regime are presented in Table 2a and we extend our findings to the full dataset in Table 2b.

**ONCE:** Furthermore, we fine-tune SECOND [63] and Centerpoint [72] on the ONCE training set. Table 4 contains our results in comparison with other pre-training methods. We outperform the state-of-the-art even without pre-training on ONCE itself. Please note that the subset  $U_{small}$  of ONCE contains 100k frames, while we pre-train on  $\sim 79k$  frames of Waymo.

In all these evaluations, we see that all baseline detectors clearly struggle if only few labels are available, especially when considering the accuracy of the estimated heading. Naturally, this is most notable for underrepresented classes, *i.e.* *Pedestrians* and *Cyclists*.

This is even more obvious if we consider the ambigu-

Fraction	Method	mAP	Car	Pedestrian	Cyclist
20% (743 frames)	PV-RCNN [63]	66.71	82.52	53.33	64.28
	+ PropCont [71]	68.13	82.65	55.05	66.68
	+ MAELi	69.41	82.21	56.71	69.30
50% (1856 frames)	PV-RCNN [63]	69.63	82.68	57.10	69.12
	+ PropCont [71]	71.76	82.92	59.92	72.45
	+ MAELi	70.13	83.89	56.48	70.02

(a) Results of our features pre-trained on Waymo and fine-tuned on different fractions of KITTI 3D.

Method	Pre-train	mAP	Car	Pedestrian	Cyclist
SECOND [63]	-	65.35	81.50	48.82	65.72
+ ALSO [3]	KITTI 3D	67.68	81.97	51.93	69.14
+ ALSO [3]	KITTI360	68.31	81.79	52.45	70.68
+ ALSO [3]	nuScenes	68.07	81.78	54.24	68.19
+ MAELi	Waymo	69.05	81.70	54.34	71.11
PV-RCNN [63]	-	70.57	84.50	57.06	70.14
+ STRL [23]	KITTI 3D	71.46	84.70	57.80	71.88
+ GCC-3D [28]	Waymo	71.26	-	-	-
+ PropCont [71]	Waymo	72.92	84.72	60.36	73.69
+ ALSO [3]	KITTI 3D	72.76	84.72	58.49	75.06
+ ALSO [3]	KITTI360	72.96	84.68	60.16	74.04
+ ALSO [3]	nuScenes	72.53	84.86	57.76	74.98
+ MAELi	Waymo	72.15	84.80	57.46	74.18

(b) Performance comparison of our features fine-tuned on the full KITTI 3D training set on SECOND and PV-RCNN.

Table 2: Quantitative results on the KITTI 3D *val* set using the standard  $R_{40}$  metric.

ous heading of an average Pedestrian’s bounding box with a nearly square footprint. However, during the reconstruction task, our features need to carefully adapt to an object’s pose, or otherwise, the reconstruction would fail. Consequently, pre-trained 3D object detectors, in particular the anchor-based SECOND and PV-RCNN, benefit from MAELi. This becomes especially evident when evaluated with orientation-aware metrics as employed by Waymo (Table 1) or ONCE (Table 4) benchmarks. For example, SECOND+MAELi gains 13.61mAPH on 10% of the

Method	3D AP/APH (LEVEL 2)									
	Gain		Overall		Vehicle		Pedestrian		Cyclist	
	AP	APH	AP	APH	AP	APH	AP	APH	AP	APH
SECOND [63]	-	-	58.26	54.35	62.58	62.02	57.22	47.49	54.97	53.53
+ Voxel-MAE [36]	+0.85	+0.75	59.11	55.10	62.67	62.34	59.03	48.79	55.62	54.17
+ MAELi	+2.32	+2.35	60.57	56.69	63.75	63.20	60.71	50.93	57.26	55.95
Centerpoint [72]	-	-	64.51	61.92	63.16	62.65	64.27	58.23	66.11	64.87
+ Voxel-MAE [36]	+1.35	+1.31	65.86	63.23	64.05	63.53	65.78	59.62	67.76	66.53
+ MAELi	+1.09	+1.08	65.60	63.00	64.22	63.70	65.93	59.79	66.66	65.52
PV-RCNN [41]	-	-	59.84	56.23	64.99	64.38	53.80	45.14	60.72	59.18
+ GCC-3D [28]	+1.46	+1.95	61.30	58.18	65.65	65.10	55.54	48.02	62.72	61.43
+ PropCont [71]	+2.78	+3.05	62.62	59.28	66.04	65.47	57.58	49.51	64.23	62.86
+ Voxel-MAE [36]	+5.99	+5.74	65.82	61.98	67.94	67.34	64.91	55.57	64.62	63.02
+ MAELi	+5.88	+5.92	65.72	62.15	67.90	67.34	65.14	56.32	64.13	62.79

Table 3: Performance comparison on the Waymo *val* set trained on 20% of the Waymo *train* set. We compare different detectors trained from scratch with their pendants utilizing pre-trained weights from GCC-3D, ProposalContrast, Voxel-MAE and MAELi.

Method	Pre-train	mAP	Orientation-Aware AP		
			Car	Pedestrian	Cyclist
SECOND [63]	-	51.89	71.19	26.44	58.04
+ SwAV [6]	$U_{small}$	51.96	72.71	25.13	58.05
+ DeepCluster [5]	$U_{small}$	52.06	73.19	24.00	58.99
+ ALSO [3]	$U_{small}$	52.68	71.73	28.16	58.13
+ MAELi	Waymo	55.84	75.86	31.03	60.65
CenterPoint [72]	-	64.24	75.26	51.65	65.79
+ PropCont [71]	Waymo	66.24	78.00	52.56	68.17
+ MAELi	Waymo	66.72	80.09	51.87	68.21

Table 4: Performance comparison on ONCE validation set. Utilizing our features, even when pre-trained on a different dataset, helps outperforming state of the art methods.

Waymo data compared to its vanilla pendant. For the full KITTI 3D dataset, ALSO [3] achieves the best performance with features pre-trained on either KITTI 3D, KITTI360 [29] or nuScenes [4]. Here, features pre-trained on Waymo also achieve top performance, as indicated by the results of ProposalContrast [71] and our MAELi. Moreover, MAELi proves especially beneficial in the targeted low-data regimes, demonstrating that only few labeled samples are needed to obtain strong detection results.

## 4.2. Improving 3D Object Detection

We also show the benefits of our expressive MAELi features by following the common protocol of using 20% of the entire Waymo *train* set including vanilla ground truth sampling to fine-tune the detectors. For this, we maintain the same pre-training as in Section 4.1 and utilize these features for SECOND [63], CenterPoint [72] and PV-RCNN [41]. Table 3 shows the results in comparison to these baseline detectors trained from scratch, as well as pre-trained with Voxel-MAE [36].

Although MAELi is tailored for data-efficiency, our self-supervised features are also able to improve the baselines

on this large amount of data. Especially for *Pedestrians*, the anchor-based methods benefit from the notion of heading to which our features inherently adapt to. Even though it is hard for a detector to estimate, this is an important cue for path prediction and collision avoidance, in particular, if we consider the vulnerability of this group in traffic.

## 4.3. Ablation Study

We conduct several experiments on the particular aspects of our pipeline. We evaluate the impact of each, the *distance weighting* for free voxels, our *LiDAR-aware reconstruction* objective and compare the masking strategies, *voxel-* and *spherical masking*.

In summary, we see that our *LiDAR-aware reconstruction* objective improves the overall results across all classes and distances and our *spherical masking* is especially beneficial for the range [30m, 50m). Detailed results and an evaluation on the fraction of masked voxels are provided in the supplementary material.

## 5. Conclusion

We proposed MAELi, a self-supervised pre-training approach, carefully designed to adapt to the inherent but subtle properties of large-scale LiDAR point clouds. We were the first to put aspects like occlusion and intrinsic spherical sampling of LiDAR data into the context of SSRL. Our learned representation is especially useful if only few labeled data is available, where it leads to significant improvements. Additionally, it can be easily applied to other datasets, again with minimal data requirements for fine-tuning. With MAELi, we offer a new method to sustainably reduce the amount of tedious and costly annotation tasks for LiDAR point clouds.



## References

- [1] Panos Achlioptas, Olga Diamanti, Ioannis Mitliagkas, and Leonidas Guibas. Learning Representations and Generative Models for 3D Point Clouds. In *Proc. ICML*, 2018. 1
- [2] Alex Bewley, Pei Sun, Thomas Mensink, Dragomir Anguelov, and Cristian Sminchisescu. Range Conditioned Dilated Convolutions for Scale Invariant 3D Object Detection. In *Proc. of Conference on Robot Learning*, 2020. 2
- [3] Alexandre Boulch, Corentin Sautier, Björn Michele, Gilles Puy, and Renaud Marlet. ALSO: Automotive Lidar Self-supervision by Occupancy estimation. *arXiv:2212.05867*, 2022. 3, 7, 8, 12, 13
- [4] Holger Caesar, Varun Bankiti, Alex H. Lang, Sourabh Vora, Venice Erin Liong, Qiang Xu, Anush Krishnan, Yu Pan, Giancarlo Baldan, and Oscar Beijbom. nuScenes: A multi-modal dataset for autonomous driving. *arXiv:1903.11027*, 2020. 8
- [5] Mathilde Caron, Piotr Bojanowski, Armand Joulin, and Matthijs Douze. Deep Clustering for Unsupervised Learning of Visual Features. In *Proc. ECCV*, 2018. 8
- [6] Mathilde Caron, Ishan Misra, Julien Mairal, Priya Goyal, Piotr Bojanowski, and Armand Joulin. Unsupervised Learning of Visual Features by Contrasting Cluster Assignments. In *Adv. NeurIPS*, 2020. 8
- [7] Angel X. Chang, Thomas Funkhouser, Leonidas Guibas, Pat Hanrahan, Qixing Huang, Zimo Li, Silvio Savarese, Manolis Savva, Shuran Song, Hao Su, Jianxiong Xiao, Li Yi, and Fisher Yu. ShapeNet: An Information-Rich 3D Model Repository. *arXiv:1512.03012*, 2015. 1, 3
- [8] Ting Chen, Simon Kornblith, Mohammad Norouzi, and Geoffrey Hinton. A Simple Framework for Contrastive Learning of Visual Representations. In *Proc. ICML*, 2020. 3
- [9] Christopher Choy, JunYoung Gwak, and Silvio Savarese. 4D Spatio-Temporal ConvNets: Minkowski Convolutional Neural Networks. In *Proc. CVPR*, 2019. 4, 5, 6
- [10] Jacob Devlin, Ming-Wei Chang, Kenton Lee, and Kristina Toutanova. BERT: Pre-training of Deep Bidirectional Transformers for Language Understanding. In *Proc. of the Conference of the North American Chapter of the Association for Computational Linguistics: Human Language Technologies*, 2019. 3
- [11] Lue Fan, Xuan Xiong, Feng Wang, Naiyan Wang, and Zhaoxiang Zhang. RangeDet: In Defense of Range View for LiDAR-based 3D Object Detection. *arXiv:2103.10039*, 2021. 2
- [12] Andreas Geiger, Philip Lenz, and Raquel Urtasun. Are we ready for autonomous driving? The KITTI vision benchmark suite. In *Proc. CVPR*, 2012. 2, 6
- [13] Rohit Girdhar, David F. Fouhey, Mikel Rodriguez, and Abhinav Gupta. Learning a Predictable and Generative Vector Representation for Objects. In *Proc. ECCV*, 2016. 3
- [14] Benjamin Graham, Martin Engelcke, and Laurens van der Maaten. 3D Semantic Segmentation With Submanifold Sparse Convolutional Networks. In *Proc. CVPR*, 2018. 4
- [15] Tianrui Guan, Jun Wang, Shiyi Lan, Rohan Chandra, Zuxuan Wu, Larry Davis, and Dinesh Manocha. M3DETR: Multi-Representation, Multi-Scale, Mutual-Relation 3D Object Detection With Transformers. In *Proc. WACV*, 2022. 2
- [16] Chenhang He, Hui Zeng, Jianqiang Huang, Xian-Sheng Hua, and Lei Zhang. Structure Aware Single-Stage 3D Object Detection From Point Cloud. In *Proc. CVPR*, 2020. 2
- [17] Kaiming He, Xinlei Chen, Saining Xie, Yanghao Li, Piotr Dollár, and Ross Girshick. Masked Autoencoders Are Scalable Vision Learners. In *Proc. CVPR*, 2022. 3
- [18] Kaiming He, Haoqi Fan, Yuxin Wu, Saining Xie, and Ross Girshick. Momentum Contrast for Unsupervised Visual Representation Learning. In *Proc. CVPR*, 2020. 3
- [19] Georg Hess, Johan Jaxing, Elias Svensson, David Hagerman, Christoffer Petersson, and Lennart Svensson. Masked Autoencoders for Self-Supervised Learning on Automotive Point Clouds. *arXiv:2207.00531*, 2022. 1, 3
- [20] R. Devon Hjelm, Alex Fedorov, Samuel Lavoie-Marchildon, Karan Grewal, Phil Bachman, Adam Trischler, and Yoshua Bengio. Learning deep representations by mutual information estimation and maximization. In *Proc. ICLR*, 2019. 3
- [21] Jordan S. K. Hu, Tianshu Kuai, and Steven L. Waslander. Point Density-Aware Voxels for LiDAR 3D Object Detection. In *Proc. CVPR*, 2022. 2
- [22] Peiyun Hu, Jason Ziglar, David Held, and Deva Ramanan. What You See is What You Get: Exploiting Visibility for 3D Object Detection. In *Proc. CVPR*, 2020. 3
- [23] Siyuan Huang, Yichen Xie, Song-Chun Zhu, and Yixin Zhu. Spatio-Temporal Self-Supervised Representation Learning for 3D Point Clouds. In *Proc. ICCV*, 2021. 3, 7
- [24] Diederik P. Kingma and Jimmy Ba. Adam: A Method for Stochastic Optimization. *arXiv:1412.6980*, 2017. 6
- [25] Alex H. Lang, Sourabh Vora, Holger Caesar, Lubing Zhou, Jiong Yang, and Oscar Beijbom. PointPillars: Fast Encoders for Object Detection From Point Clouds. In *Proc. CVPR*, 2019. 2
- [26] Bo Li, Tianlei Zhang, and Tian Xia. Vehicle Detection from 3D Lidar Using Fully Convolutional Network. In *Robotics: Science and Systems*, 2016. 2
- [27] Zhichao Li, Feng Wang, and Naiyan Wang. LiDAR R-CNN: An Efficient and Universal 3D Object Detector. In *Proc. CVPR*, 2021. 2
- [28] Hanxue Liang, Chenhan Jiang, Dapeng Feng, Xin Chen, Hang Xu, Xiaodan Liang, Wei Zhang, Zhenguo Li, and Luc Van Gool. Exploring Geometry-Aware Contrast and Clustering Harmonization for Self-Supervised 3D Object Detection. In *Proc. ICCV*, 2021. 3, 7, 8
- [29] Yiyi Liao, Jun Xie, and Andreas Geiger. KITTI-360: A Novel Dataset and Benchmarks for Urban Scene Understanding in 2D and 3D, 2022. 8
- [30] Haotian Liu, Mu Cai, and Yong Jae Lee. Masked Discrimination for Self-Supervised Learning on Point Clouds. In *Proc. ECCV*, 2022. 1, 3
- [31] Jiageng Mao, Minzhe Niu, Haoyue Bai, Xiaodan Liang, Hang Xu, and Chunjing Xu. Pyramid R-CNN: Towards Better Performance and Adaptability for 3D Object Detection. In *Proc. ICCV*, 2021. 2
- [32] Jiageng Mao, Minzhe Niu, Chenhan Jiang, Hanxue Liang, Jingheng Chen, Xiaodan Liang, Yamin Li, Chaoqiang Ye,

- Wei Zhang, Zhenguo Li, Jie Yu, Hang Xu, and Chunjing Xu. One Million Scenes for Autonomous Driving: ONCE Dataset. *arXiv:2106.11037*, arXiv:2106.11037, 2021. 2, 6
- [33] Jiageng Mao, Yujing Xue, Minzhe Niu, Haoyue Bai, Jiashi Feng, Xiaodan Liang, Hang Xu, and Chunjing Xu. Voxel Transformer for 3D Object Detection. In *Proc. ICCV*, 2021. 2
- [34] Gregory P. Meyer, Ankit Laddha, Eric Kee, Carlos Vallespi-Gonzalez, and Carl K. Wellington. LaserNet: An Efficient Probabilistic 3D Object Detector for Autonomous Driving. In *Proc. CVPR*, 2019. 2
- [35] Zhenwei Miao, Jikai Chen, Hongyu Pan, Ruiwen Zhang, Kaixuan Liu, Peihan Hao, Jun Zhu, Yang Wang, and Xin Zhan. PVGNet: A Bottom-Up One-Stage 3D Object Detector With Integrated Multi-Level Features. In *Proc. CVPR*, 2021. 2
- [36] Chen Min, Xinli Xu, Dawei Zhao, Liang Xiao, Yiming Nie, and Bin Dai. Voxel-MAE: Masked Autoencoders for Pre-training Large-scale Point Clouds. *arXiv:2206.09900*, 2022. 1, 3, 8, 12, 13
- [37] Yatian Pang, Wenxiao Wang, Francis E. H. Tay, Wei Liu, Yonghong Tian, and Li Yuan. Masked Autoencoders for Point Cloud Self-supervised Learning. In *Proc. ECCV*, 2022. 1, 3, 6
- [38] Charles R. Qi, Hao Su, Kaichun Mo, and Leonidas J. Guibas. PointNet: Deep Learning on Point Sets for 3D Classification and Segmentation. In *Proc. CVPR*, 2017. 2
- [39] Charles Ruizhongtai Qi, Li Yi, Hao Su, and Leonidas J. Guibas. PointNet++: Deep Hierarchical Feature Learning on Point Sets in a Metric Space. In *Adv. NeurIPS*, 2017. 2
- [40] Hualian Sheng, Sijia Cai, Yuan Liu, Bing Deng, Jianqiang Huang, Xian-Sheng Hua, and Min-Jian Zhao. Improving 3D Object Detection With Channel-Wise Transformer. In *Proc. ICCV*, 2021. 2
- [41] Shaoshuai Shi, Chaoxu Guo, Li Jiang, Zhe Wang, Jianping Shi, Xiaogang Wang, and Hongsheng Li. PV-RCNN: Point-Voxel Feature Set Abstraction for 3D Object Detection. In *Proc. CVPR*, 2020. 2, 8, 12, 13
- [42] Shaoshuai Shi, Li Jiang, Jiajun Deng, Zhe Wang, Chaoxu Guo, Jianping Shi, Xiaogang Wang, and Hongsheng Li. PV-RCNN++: Point-Voxel Feature Set Abstraction With Local Vector Representation for 3D Object Detection. *arXiv:2102.00463*, 2022. 2
- [43] Shaoshuai Shi, Xiaogang Wang, and Hongsheng Li. PointRCNN: 3D Object Proposal Generation and Detection From Point Cloud. In *Proc. CVPR*, 2019. 2
- [44] Shaoshuai Shi, Zhe Wang, Jianping Shi, Xiaogang Wang, and Hongsheng Li. From Points to Parts: 3D Object Detection From Point Cloud With Part-Aware and Part-Aggregation Network. *PAMI*, 43(08):2647–2664, 2021. 2, 4
- [45] Weijing Shi and Raj Rajkumar. Point-GNN: Graph Neural Network for 3D Object Detection in a Point Cloud. In *Proc. CVPR*, 2020. 2
- [46] Leslie N. Smith. A disciplined approach to neural network hyper-parameters: Part 1 – learning rate, batch size, momentum, and weight decay. *arXiv:1803.09820*, 2018. 6
- [47] Pei Sun, Henrik Kretschmar, Xerxes Dotiwalla, Aurelien Chouard, Vijaysai Patnaik, Paul Tsui, James Guo, Yin Zhou, Yuning Chai, Benjamin Caine, Vijay Vasudevan, Wei Han, Jiquan Ngiam, Hang Zhao, Aleksei Timofeev, Scott Ettinger, Maxim Krivokon, Amy Gao, Aditya Joshi, Yu Zhang, Jonathon Shlens, Zhifeng Chen, and Dragomir Anguelov. Scalability in Perception for Autonomous Driving: Waymo Open Dataset. In *Proc. CVPR*, 2020. 1, 2, 6
- [48] Pei Sun, Mingxing Tan, Weiyue Wang, Chenxi Liu, Fei Xia, Zhaoqi Leng, and Dragomir Anguelov. SWFormer: Sparse Window Transformer for 3D Object Detection in Point Clouds. In *Proc. ECCV*, 2022. 2
- [49] OpenPCDet Development Team. OpenPCDet: An Open-source Toolbox for 3D Object Detection from Point Clouds. <https://github.com/open-mmlab/OpenPCDet>, 2020. 6
- [50] Darren Tsai, Julie Stephany Berrio, Mao Shan, Eduardo Nebot, and Stewart Worrall. Viewer-Centred Surface Completion for Unsupervised Domain Adaptation in 3D Object Detection. *arXiv:2209.06407*, 2022. 3
- [51] Ashish Vaswani, Noam Shazeer, Niki Parmar, Jakob Uszkoreit, Llion Jones, Aidan N Gomez, Łukasz Kaiser, and Illia Polosukhin. Attention is All you Need. In *Adv. NeurIPS*, 2017. 2
- [52] Hanchen Wang, Qi Liu, Xiangyu Yue, Joan Lasenby, and Matt J. Kusner. Unsupervised Point Cloud Pre-Training via Occlusion Completion. In *Proc. ICCV*, 2021. 1, 3
- [53] Wenguan Wang, Tianfei Zhou, Fisher Yu, Jifeng Dai, Ender Konukoglu, and Luc Van Gool. Exploring Cross-Image Pixel Contrast for Semantic Segmentation. In *Proc. ICCV*, 2021. 3
- [54] Yan Wang, Xiangyu Chen, Yurong You, Li Erran Li, Bharath Hariharan, Mark Campbell, Kilian Q. Weinberger, and Wei-Lun Chao. Train in Germany, Test in the USA: Making 3D Object Detectors Generalize. In *Proc. CVPR*, 2020. 1
- [55] Yue Wang, Alireza Fathi, Abhijit Kundu, David A. Ross, Caroline Pantofaru, Tom Funkhouser, and Justin Solomon. Pillar-Based Object Detection for Autonomous Driving. In *Proc. ECCV*, 2020. 2
- [56] Xin Wen, Tianyang Li, Zhizhong Han, and Yu-Shen Liu. Point Cloud Completion by Skip-Attention Network With Hierarchical Folding. In *Proc. CVPR*, 2020. 1
- [57] Zhirong Wu, Shuran Song, Aditya Khosla, Fisher Yu, Linguang Zhang, Xiaoou Tang, and Jianxiong Xiao. 3D ShapeNets: A Deep Representation for Volumetric Shapes. In *Proc. CVPR*, 2015. 1, 3
- [58] Guangda Xie, Yang Li, Hongquan Qu, and Zaiming Sun. Masked Autoencoder for Pre-Training on 3D Point Cloud Object Detection. *Mathematics*, 10(19):3549, 2022. 3
- [59] Saining Xie, Jiatao Gu, Demi Guo, Charles R. Qi, Leonidas Guibas, and Or Litany. PointContrast: Unsupervised Pre-training for 3D Point Cloud Understanding. In *Proc. ECCV*, 2020. 3
- [60] Qiangeng Xu, Yiqi Zhong, and Ulrich Neumann. Behind the Curtain: Learning Occluded Shapes for 3D Object Detection. In *Proc. AAAI*, 2022. 3

- [61] Qiangeng Xu, Yin Zhou, Weiyue Wang, Charles R. Qi, and Dragomir Anguelov. SPG: Unsupervised Domain Adaptation for 3D Object Detection via Semantic Point Generation. In *Proc. ICCV*, 2021. 3
- [62] Siming Yan, Zhenpei Yang, Haoxiang Li, Li Guan, Hao Kang, Gang Hua, and Qixing Huang. Implicit Autoencoder for Point Cloud Self-supervised Representation Learning. *arXiv:2201.00785*, 2022. 3
- [63] Yan Yan, Yuxing Mao, and Bo Li. SECOND: Sparsely Embedded Convolutional Detection. *Sensors*, 18(10):3337, 2018. 2, 3, 4, 6, 7, 8, 12, 13, 14, 16, 17
- [64] Bin Yang, Wenjie Luo, and Raquel Urtasun. PIXOR: Real-Time 3D Object Detection From Point Clouds. In *Proc. CVPR*, 2018. 2
- [65] Honghui Yang, Tong He, Jiaheng Liu, Hua Chen, Boxi Wu, Binbin Lin, Xiaofei He, and Wanli Ouyang. GD-MAE: Generative Decoder for MAE Pre-training on LiDAR Point Clouds. *arXiv:2212.03010*, arXiv:2212.03010, 2022. 2
- [66] Juyoung Yang, Pyunghwan Ahn, Doyeon Kim, Haeil Lee, and Junmo Kim. Progressive Seed Generation Auto-Encoder for Unsupervised Point Cloud Learning. In *Proc. ICCV*, 2021. 3
- [67] Zetong Yang, Yanan Sun, Shu Liu, and Jiaya Jia. 3DSSD: Point-Based 3D Single Stage Object Detector. In *Proc. CVPR*, 2020. 2
- [68] Zetong Yang, Yanan Sun, Shu Liu, Xiaoyong Shen, and Jiaya Jia. STD: Sparse-to-Dense 3D Object Detector for Point Cloud. In *Proc. ICCV*, 2019. 2
- [69] Maosheng Ye, Shuangjie Xu, and Tongyi Cao. HVNet: Hybrid Voxel Network for LiDAR Based 3D Object Detection. In *Proc. CVPR*, 2020. 2
- [70] Junbo Yin, Jin Fang, Dingfu Zhou, Liangjun Zhang, Cheng-Zhong Xu, Jianbing Shen, and Wenguan Wang. Semi-supervised 3D Object Detection with Proficient Teachers. In *Proc. ECCV*, 2022. 7
- [71] Junbo Yin, Dingfu Zhou, Liangjun Zhang, Jin Fang, Cheng-Zhong Xu, Jianbing Shen, and Wenguan Wang. Proposal-Contrast: Unsupervised Pre-training for LiDAR-based 3D Object Detection. In *Proc. ECCV*, 2022. 3, 7, 8
- [72] Tianwei Yin, Xingyi Zhou, and Philipp Krähenbühl. Center-Based 3D Object Detection and Tracking. In *Proc. CVPR*, 2021. 2, 7, 8, 12, 13
- [73] Xumin Yu, Lulu Tang, Yongming Rao, Tiejun Huang, Jie Zhou, and Jiwen Lu. Point-BERT: Pre-Training 3D Point Cloud Transformers With Masked Point Modeling. In *Proc. CVPR*, 2022. 1, 3, 6
- [74] Yifan Zhang, Qingyong Hu, Guoquan Xu, Yanxin Ma, Jianwei Wan, and Yulan Guo. Not All Points Are Equal: Learning Highly Efficient Point-Based Detectors for 3D LiDAR Point Clouds. In *Proc. CVPR*, 2022. 2
- [75] Zaiwei Zhang, Rohit Girdhar, Armand Joulin, and Ishan Misra. Self-Supervised Pretraining of 3D Features on Any Point-Cloud. In *Proc. ICCV*, 2021. 3
- [76] Xingyi Zhou, Dequan Wang, and Philipp Krähenbühl. Objects as Points. *arXiv:1904.07850*, 2019. 2
- [77] Yin Zhou and Oncel Tuzel. VoxelNet: End-to-End Learning for Point Cloud Based 3D Object Detection. In *Proc. CVPR*, 2018. 2

# Supplementary Material

This supplementary material presents further details, results and insights into MAELi. We state further results in Appendix A, describe the detailed architecture of our decoder in Appendix B and illustrate the motivation behind spherical masking in Appendix C. Furthermore, we evaluate the impact of different amounts of masked voxels in Appendix D and discuss potential limitations in Appendix E. Finally, we discuss some additional insights on reconstruction results and data efficiency in Appendix F.

## A. Additional Results

We provide results for CenterPoint [72] and PV-RCNN [41] to demonstrate that our pre-trained features, again, greatly enhance these baselines. Following the insights from the main manuscript (Section 4.1), we also see for these other detectors in Table S1 that our MAELi features are highly effective to enable good detection performance in the low-data regime, where only few annotated samples are available for fine-tuning. Additionally, in Table S2, we present our results on the KITTI 3D dataset using the  $R_{11}$  metric and compare with ALSO [3] and Voxel-MAE [36].

## B. Sparse Reconstruction Decoder

To describe the architecture of our decoder in detail, we group operations with the same *voxel/tensor stride* into a *block*. In Table S3, we list the different decoder blocks in addition to the preceding SECOND [63] encoder (summarized as single entry) and the required *reshaping+sampling* step to transform the dense feature representation back to a sparse 3D tensor.

Each block consists, among others, of an upsampling- and pruning step. For upsampling, we utilize a *generative transposed convolution* and for pruning, we use a  $1 \times 1 \times 1$  submanifold sparse convolution to create the required classification score. The respective operations of each block are listed in Table S4.

## C. Spherical Masking - Illustration

As discussed in the main paper (Section 3.4), spherical masking reduces the angular resolution in azimuth and inclination by subsampling the LiDAR’s range image. Figure S1 illustrates the effect of this sampling on the LiDAR’s range image. We sample objects as if they were located at a larger distance. Since nearby objects are more densely sensed by the LiDAR, we have more knowledge about the actual occupancy and thus, can induce a stronger self-supervision signal. This helps to improve the model’s ability to generalize to objects located farther away.

## D. Ablation Study - Details

**Analyzing Pipeline Components:** We perform various experiments to investigate specific aspects of our pipeline, such as assessing the influence of our *distance weighting* for free voxels, evaluating our *LiDAR-aware reconstruction* objective, and comparing the effectiveness of the *voxel-* and *spherical masking* strategies.

Therefore, we pre-train according to the protocol depicted in the main paper (Section 4.1) and fine-tune a SECOND [63] model on 1% of the latter 399 sequences of the Waymo *train* set. To disable *distance weighting*, we set  $w_j^{D,s} = 1$  for all *free* voxels  $\mathbf{v}_j^{D,s}$ . To disable our *LiDAR-aware reconstruction*, we additionally consider all *unknown* voxels as *free*.

We state the results in Table S5 on *Vehicle* LEVEL 2 across the distance ranges [0m, 30m), [30m, 50m) and [50m,  $+\infty$ ). Our *LiDAR-aware reconstruction* objective improves the overall results across all classes. While *voxel masking* naturally has a nearly equal impact over all ranges, our *spherical masking* is especially beneficial for the range [30m, 50m) with a gain of 1.87AP and 2.01APH. The overall lower impact on the far distance range (above 50m) is also reasonable, since at this distance only very few points are sampled on the same object.

**Masking:** We evaluated our *voxel masking* under different amounts of voxels. We maintain the training and evaluation scheme from above and vary the amount of kept voxels. The results are shown in Table S6. Overall, keeping 60% of the

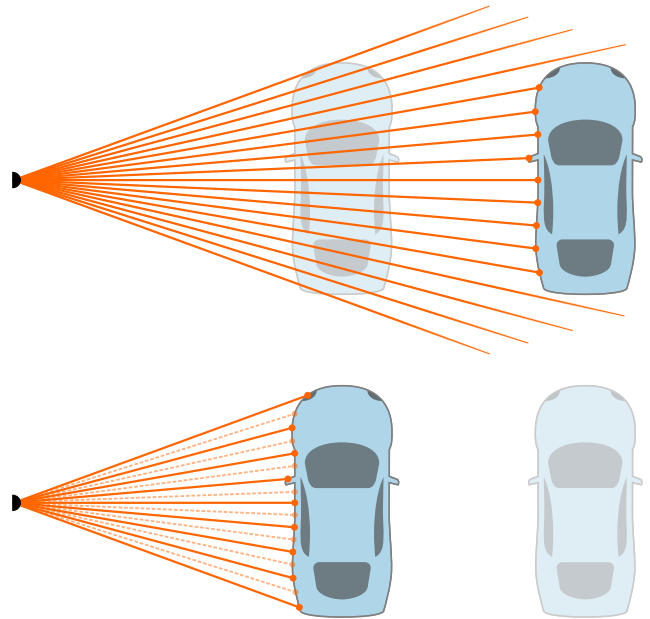


Figure S1: Spherical masking reduces the angular resolution of the LiDAR (bottom). The resulting sampling is thus similar to objects that are farther away (top).



Fraction	Method	3D AP/APH (LEVEL 2)									
		Gain		Overall		Vehicle		Pedestrian		Cyclist	
		AP	APH	AP	APH	AP	APH	AP	APH	AP	APH
1% (791 frames)	Centerpoint [72]	-	-	39.64	36.50	41.01	40.32	40.01	32.63	37.90	36.55
	+ MAELi	+9.29	+8.75	48.93	45.25	49.99	49.24	51.92	43.07	44.89	43.43
	PV-RCNN [41]	-	-	43.93	30.72	51.34	48.70	41.59	20.35	38.86	23.11
	+ MAELi	+7.53	+4.89	51.46	35.61	56.24	55.38	49.41	25.32	48.73	26.14
5% (3952 frames)	Centerpoint [72]	-	-	53.91	51.16	53.04	52.45	52.73	46.51	55.96	54.53
	+ MAELi	+4.49	+4.21	58.40	55.37	57.62	57.01	59.01	51.83	58.57	57.27
	PV-RCNN [41]	-	-	56.98	38.98	61.66	60.86	53.28	27.15	56.00	28.92
	+ MAELi	+1.64	+1.39	58.62	40.37	62.77	62.04	57.07	29.05	56.02	30.02
10% (7904 frames)	Centerpoint [72]	-	-	58.09	55.41	56.95	56.40	56.97	50.90	60.35	58.94
	+ MAELi	+3.26	+3.07	61.35	58.48	59.93	59.36	62.06	55.30	62.06	60.78
	PV-RCNN [41]	-	-	60.09	41.89	63.73	63.05	57.32	30.09	59.23	32.53
	+ MAELi	+1.19	-0.05	61.28	41.84	64.63	63.99	59.82	30.90	59.40	30.62
20% (15808 frames)	Centerpoint [72]	-	-	61.81	59.15	60.59	60.06	61.19	55.03	63.64	62.36
	+ MAELi	+0.98	+0.90	62.79	60.05	61.79	61.23	63.47	57.04	63.11	61.87
	PV-RCNN [41]	-	-	62.15	42.99	65.01	64.35	60.40	30.30	61.05	34.32
	+ MAELi	+0.49	+7.21	62.65	50.20	65.45	64.85	61.54	35.52	60.95	50.24

Table S1: Quantitative results of our features on Centerpoint and PV-RCNN on the Waymo *val* set. For each detector, we report the results of training from scratch (upper row) and the improved results utilizing MAELi-pre-trained features (lower row), respectively. We use the first 399 sequences of the Waymo *train* set for pre-training and different fractions of the second 399 sequences for fine-tuning.

Method	Pre-train	mAP	Car	Pedestrian	Cyclist
SECOND [63]	-	66.25	78.62	52.98	67.15
+ Voxel-MAE [36]	KITTI 3D	66.71	78.90	53.14	68.08
+ ALSO [3]	KITTI 3D	66.86	78.78	53.57	68.22
+ ALSO [3]	KITTI360	67.40	78.63	54.23	69.35
+ ALSO [3]	nuScenes	67.29	78.65	55.17	68.05
+ MAELi	Waymo	68.31	78.44	55.72	70.78
PV-RCNN [41]	-	70.66	83.61	57.90	70.47
+ Voxel-MAE [36]	KITTI 3D	71.73	83.82	59.37	71.99
+ ALSO [3]	KITTI 3D	71.96	83.67	58.48	73.74
+ ALSO [3]	KITTI360	72.69	83.39	60.83	73.85
+ ALSO [3]	nuScenes	72.20	83.77	58.49	74.35
+ MAELi	Waymo	71.79	83.38	58.53	73.45

Table S2: Quantitative results of our features on SECOND and PV-RCNN on the KITTI 3D *val* set using the  $R_{11}$  metric.

voxels lead to the best overall results, eventually used for all other experiments with MAELi. However, in combination with *spherical masking* significantly fewer points than this fraction actually remain. To get an estimate, we evaluated the amount of effectively used points over 10000 iterations, resulting in a fraction of 15.57% on average.

## E. Limitations

Even though our sparse decoder allows for a memory efficient reconstruction, the amount of reconstructed voxels is obviously constrained by the available compute infras-

tructure. Especially during the first iterations of our pre-training, while not sufficiently trained, some samples may lead to an uncontrolled reconstruction. In order to regulate the amount of reconstructed voxels and to avoid training breakdowns, we introduce two limiting factors. First, we prune all reconstructed voxels 0.1m below the ego vehicle, since these are below the ground plane and thus, typically provide no useful contribution. Second, we introduce a threshold for the maximum amount of reconstructed voxels to ensure that we do not run into memory issues. If an upsampling step would generate more voxels than

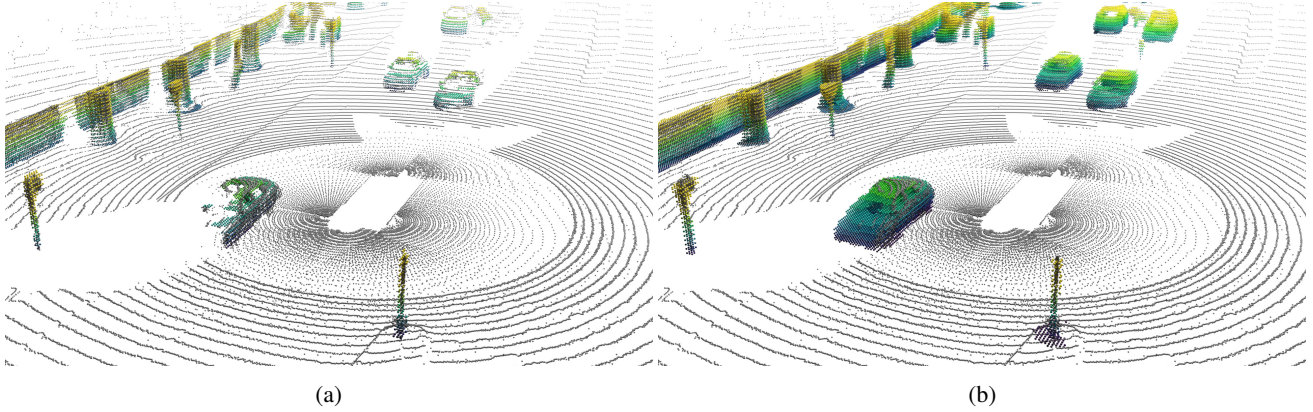


Figure S2: Completion results a) without and b) with our *LiDAR-aware reconstruction* on a full point cloud (gray). For visualization purposes, we color-coded the output points by their  $z$ -coordinate and removed the reconstructed ground plane.

Description	# Channels	Voxel/Tensor Stride	Spatial Dimension
SECOND Encoder	512	-	$188 \times 188$
Reshaping + Sampling	256	$8 \times 8 \times 16$	$188 \times 188 \times 2$
DBlock 1	64	$8 \times 8 \times 8$	$188 \times 188 \times 5$
DBlock 2	64	$4 \times 4 \times 4$	$376 \times 376 \times 11$
DBlock 3	32	$2 \times 2 \times 2$	$752 \times 752 \times 21$
DBlock 4	16	$1 \times 1 \times 1$	$1504 \times 1504 \times 41$

Table S3: Architecture of our decoder. We state the number of channels, the voxel stride and the maximum spatial dimension for the Waymo *after* each block. Stride and spatial dimensions are depicted in the format  $x \times y \times z$ . Each decoder block *inverts* one downsampling step from the encoder, eventually resulting in the original voxel stride.

Operation	Kernel Size	Stride
Generative Transposed Convolution	$2 \times 2 \times 2^\dagger$	$2 \times 2 \times 2^\dagger$
Batch Norm	-	-
ReLU	-	-
Submanifold Sparse Convolution	$3 \times 3 \times 3$	$1 \times 1 \times 1$
Batch Norm	-	-
ReLU	-	-
Submanifold Sparse Convolution	$1 \times 1 \times 1$	$1 \times 1 \times 1$
Pruning	-	-

Table S4: Structure of each decoder block. We additionally state the operation’s kernel size and stride, each in the format  $x \times y \times z$ . The upper part depicts the upsampling and feature transformation. The lower part uses the final feature representation from above and decides via classification whether a voxels is pruned or not.  $^\dagger$ These values deviate for DBlock 1, where it has a kernel size of  $1 \times 1 \times 3$  and a stride of  $1 \times 1 \times 2$  to invert the encoder’s respective downsampling step.

this limit, we randomly prune before the upsampling. For these pruned voxels, simply no loss is induced, which only slightly *delays* the training effect for these rare cases. We set the maximum number of total voxels to 6 million, which are easily processable on an NVIDIA® GeForce® RTX 3090 GPU and counted only 62 limit exceedances within the first 10k iterations of a random experiment.

## F. Additional Insights

**Reconstruction Capabilities:** In Figure S2, we visualize the completion capabilities of our *LiDAR-aware loss* on a full point cloud. It encourages the network to fill up gaps in the wall and reconstruct the occluded areas of cars.

Figure S3 highlights that reconstruction outcomes can vary across different objects, with some objects such as the less frequent trucks presenting greater challenges. However, the MAELi model demonstrates an advanced understanding of object semantics, enabling it to complete objects beyond the visible LiDAR input point cloud.

In Figure S4, we show the individual layers of two different reconstructed cars. We can see that our pretraining scheme indeed encourages the model to go beyond the sampled LiDAR surface, reconstructing the entire car, also showing some hints for the correct placement of tires. Furthermore, especially parts of the interior, which are often surrounded by glass and thus, sometimes traversed by LiDAR beams, are seemingly left out during the reconstruction.

**AP vs APH Data Efficiency:** In Figure S5, we plot the data efficiency results using our MAELi-based pre-training on the SECOND [63] detector. All three classes benefit from our pre-training (solid lines) compared to the vanilla version trained from scratch (dotted lines). With little data, the vanilla detector especially struggles

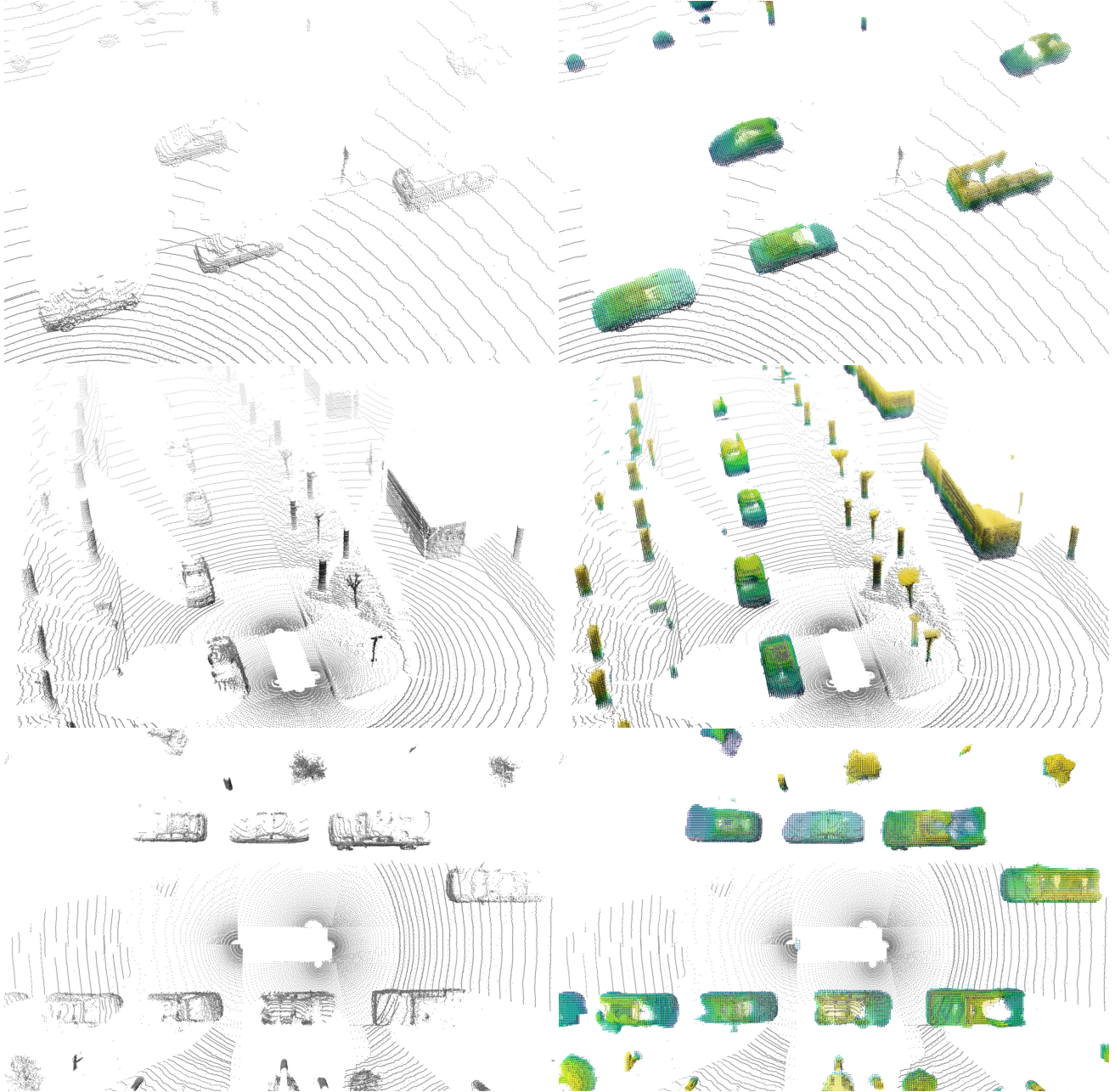


Figure S3: Further reconstruction results. We show the input point cloud on the left and the completed point cloud on the right. MAELi’s reconstruction exhibits imperfections when reconstructing objects that are sparsely sampled or less frequent, such as trucks. However, it shows an apparent understanding of traffic scenes beyond a LiDAR’s 2.5D sampling, *e.g.* by symmetrically completing occluded parts of cars and poles. For visualization purposes, we color-coded the output points by their  $z$ -coordinate and removed the reconstructed ground plane.

to estimate the heading, which can be clearly seen for the smaller, less represented classes *Pedestrian* and *Cyclist*. However, utilizing our features, a proper estimation and significant detection improvements are possible already, early on, with only few annotated data samples.

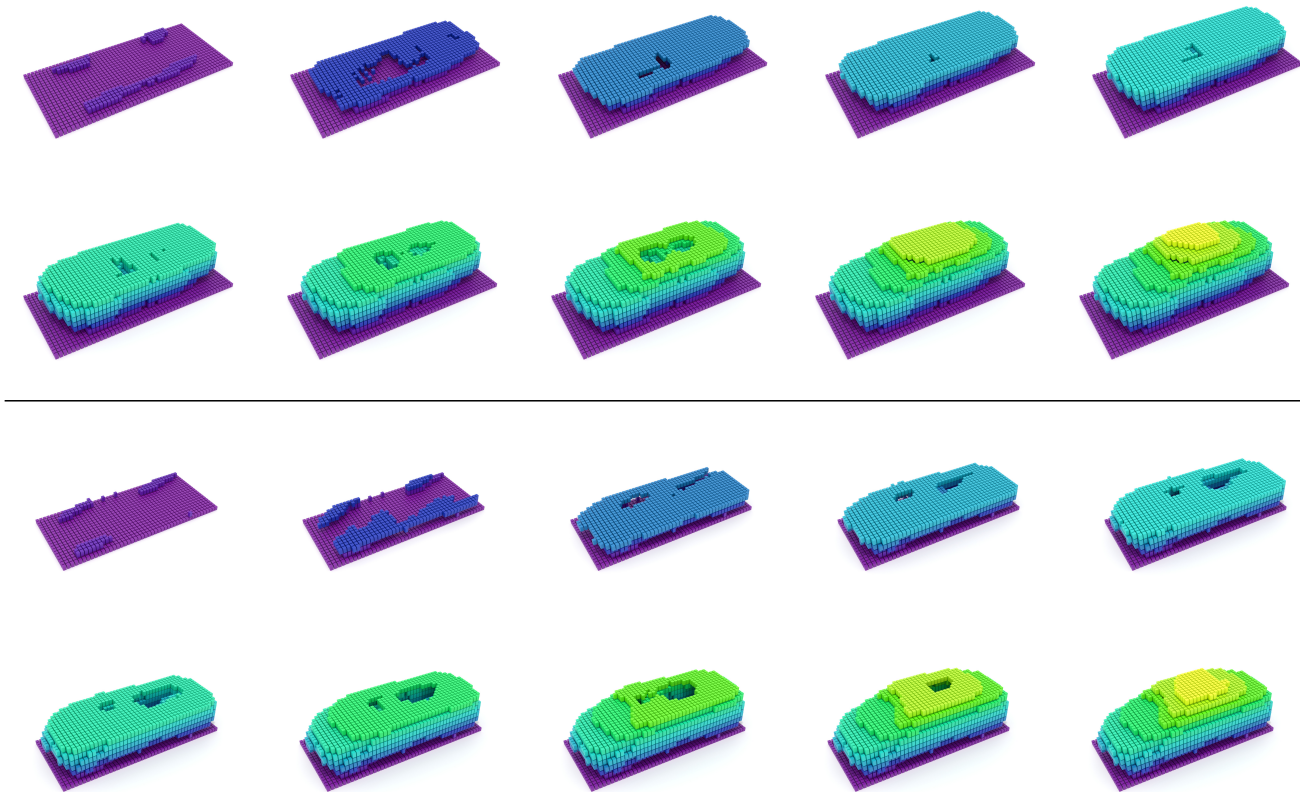


Figure S4: Different layers of two reconstructed cars. We observed, that the reconstructed cars are often hollow. There are visible tendencies to leave parts of the interior free.

Method	3D AP/APH (LEVEL 2)							
	Overall		[0m, 30m)		[30m, 50m)		[50m, +inf)	
	AP	APH	AP	APH	AP	APH	AP	APH
MAELi	51.05	50.11	80.22	79.37	48.86	47.64	21.09	19.98
w/o DW	50.91	49.85	79.95	79.04	48.62	47.20	21.47	20.31
w/o LAR	50.05	48.87	79.33	78.20	47.77	46.27	20.66	19.56
w/o VM	48.99	47.86	78.45	77.46	46.43	45.05	19.47	18.23
w/o SM	49.90	48.85	79.50	78.54	46.99	45.63	20.53	19.37
Baseline	41.64	40.02	72.59	70.79	37.09	34.86	13.14	11.96

Table S5: Impact of the components of MAELi evaluated on the Waymo *val* set for *Vehicle*. We disable *distance weighting* (w/o DW), *LiDAR-aware reconstruction* (w/o LAR), *voxel masking* (w/o VM) and *spherical masking* (w/o SM). We use the first 399 sequences of the Waymo *train* set for pre-training and 1% of the second 399 sequences for fine-tuning. We utilize a SECOND [63] model and state a version trained from scratch as baseline.



Fraction Voxels	3D AP/APH (LEVEL 2)							
	Overall		Vehicle		Pedestrian		Cyclist	
	AP	APH	AP	APH	AP	APH	AP	APH
0.8	45.34	32.84	50.26	49.10	48.03	24.33	37.74	25.09
0.7	44.91	32.10	50.35	49.19	47.54	24.29	36.83	22.83
0.6	46.01	33.05	51.05	50.11	48.13	24.65	38.86	24.38
0.5	45.60	32.27	50.87	49.79	47.08	23.72	38.86	23.31
0.4	45.79	31.85	50.36	49.24	48.27	24.50	38.74	21.81
Baseline	31.09	22.25	41.64	40.02	33.39	17.45	18.24	9.29

Table S6: Impact of different amounts of voxels kept during *voxel masking* evaluated on the Waymo *val* set for *Vehicle*. We use the first 399 sequences of the Waymo *train* set for pre-training and 1% of the second 399 sequences for fine-tuning. We utilize a SECOND [63] model and state a version trained from scratch as baseline.

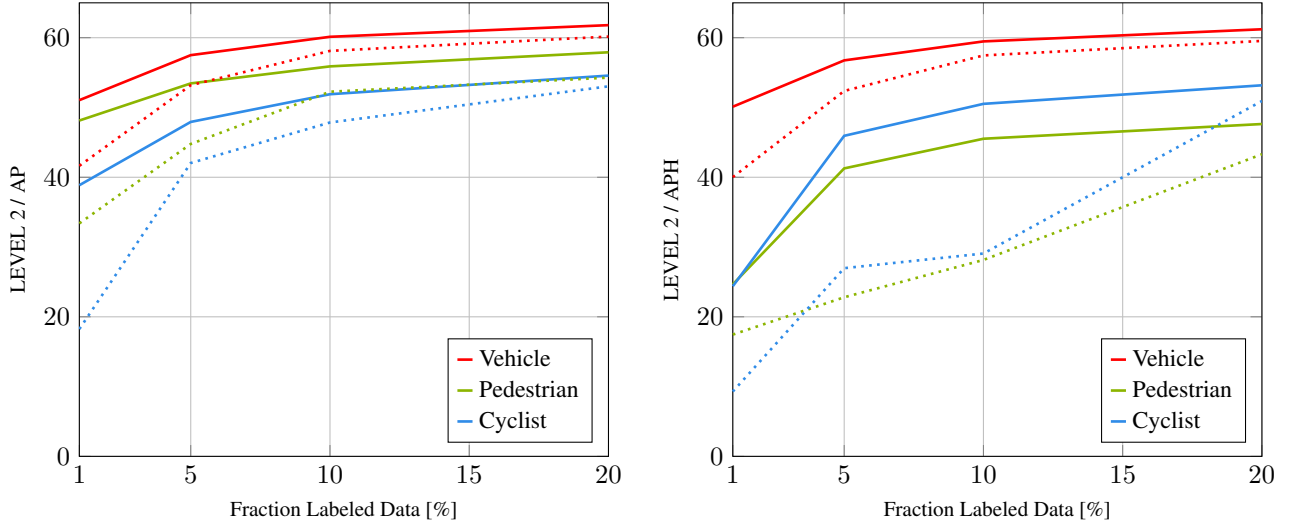


Figure S5: Results of our features on SECOND [63] on the Waymo *val* set, using different amounts of labeled data. We use the first 399 sequences of the Waymo *train* set without any labels for pre-training and different fractions of the latter 399 sequences for fine-tuning. The *solid lines* are the results utilizing our features pre-trained with MAELi. The *dotted lines* denote the version trained from scratch.